

FULL PAPER

Open Access



Unmodelled magnetic contributions in satellite-based models

Roberta Tozzi^{1*} , Mioara Manda² and Paola De Michelis¹

Abstract

A complex system of electric currents flowing in the ionosphere and magnetosphere originates from the interaction of the solar wind and the Interplanetary Magnetic Field (IMF) with the Earth's magnetic field. These electric currents generate magnetic fields contributing themselves to those measured by both ground observatories and satellites. Here, low-resolution (1 Hz) magnetic vector data recorded between 1 March 2014 and 31 May 2015 by the recently launched Swarm constellation are considered. The core and crustal magnetic fields and part of that originating in the magnetosphere are removed from Swarm measurements using CHAOS-5 model. Low- and mid-latitude residuals of the geomagnetic field representing the ionospheric and the unmodelled magnetospheric contributions are investigated, in the Solar Magnetic frame, according to the polarity of IMF B_y (azimuthal) and B_z (north–south) components and to different geomagnetic activity levels. The proposed approach makes it possible to investigate the features of unmodelled contributions due to the external sources of the geomagnetic field. Results show, on one side, the existence of a relation between the analysed residuals and IMF components B_y and B_z , possibly due to the long distance effect of high-latitude field-aligned currents. On the other side, they suggest the presence of a contribution due to the partial ring current that is activated during the main phase of geomagnetic storms. The perturbation observed on residuals is also compatible with the effect of the net field-aligned currents. Moreover, we have quantitatively estimated the effect of these current systems on computed residuals.

Keywords: Swarm magnetic vector data, Interplanetary Magnetic Field, Magnetic models, Field-aligned currents, Partial ring current

Introduction

Swarm mission

To thoroughly investigate the Earth's magnetic field, it is crucial to adopt an observation strategy that identifies the contributions due to the different sources. The Swarm mission was designed as a constellation of three satellites, offering then the possibility to study the signal generated by the core, the mantle, the lithosphere, the ionosphere and the magnetosphere, and perhaps even by the ocean currents. This mission takes over from the German CHAMP satellite (2000–2010), which carried a comparable set of instruments, and the Danish Ørsted satellite, launched in 1999, whose scalar magnetometer

has continued providing some measurements, on an irregular timescale, until 2013.

Launched on 22 November 2013, this European Space Agency (ESA) mission is devoted to the study of the geomagnetic field and its interactions with the Earth's system (Christensen et al. 2006). The main objectives of the Swarm mission are to deliver the best survey of the geomagnetic field and its temporal variation and to obtain a space–time characterisation of both the internal field sources in the Earth and the ionospheric–magnetospheric current systems. The mission was designed to derive the first global representation of the geomagnetic field variations on timescales from an hour to several years, addressing the crucial problem of source separation.

The three Swarm satellites are identical, and the constellation consists of two satellites (A and C) flying almost side by side at an altitude close to 460 km (April 2016),

*Correspondence: roberta.tozzi@ingv.it

¹ Istituto Nazionale di Geofisica e Vulcanologia, Via di Vigna Murata 605, 00143 Rome, Italy

Full list of author information is available at the end of the article

longitude separation of 1.4° and on circular and almost polar orbits with an inclination of 87.4° . The third satellite (B) flies above, close to 510 km (April 2016), on a more polar orbit (inclination of 87.8°) and is allowed for a progressive Local Time (LT) separation with respect to A and C, of about 3 h on January 2016.

The instrument that we are interested in and use the data is mainly the Vector Field Magnetometer (VFM), mounted halfway along the boom on an optical bench together with the Star Trackers (STR). The instrument is a 3-axis Compact Spherical Coil (CSC). It is an analogue instrument and as such subject to temporal changes of the electronics due to radiation and ageing effects. These effects are estimated on a daily basis by comparison between the VFM with the Absolute Scalar Magnetometer (ASM) outputs.

Magnetic field, navigation, accelerometer, plasma and electric field measurements are provided by ESA as Level 1b data, which consist of calibrated and formatted time series of the observations. The Level 1b data are provided individually for each satellite on a daily basis.

Earth's magnetic field contributions

As mentioned above, Swarm magnetometers measure a superposition of magnetic fields produced by a number of different sources: core, lithosphere, ionosphere and magnetosphere. Core magnetic field dominates over the fields produced by the other sources; it varies in time on scales longer than a month. At satellite altitude, with the exception of large magnetic anomalies, the lithospheric magnetic field is of the order of a few nanoTeslas and in most cases it can be considered constant in time (Thébault et al. 2009).

Contributions due to external sources depend largely on latitude, local time and solar activity. At low and mid-latitudes, most intense contributions from the ionosphere are produced by the currents flowing in the E region during daytime, i.e. the solar quiet current and the eastward equatorial electrojet. At these latitudes night-time currents are much weaker (around three orders of magnitude less) than those observed during the day; nonetheless, they produce still measurable contributions (e.g. Park et al. 2009). At the poles the most intense ionospheric contributions are given by the auroral electrojets and by the field-aligned currents (FAC).

Among the magnetospheric sources, the ring current is dominant at low and mid-latitudes, even if some other faraway sources should be considered, for instance magnetopause and cross-tail currents. At satellite altitude, the ring current is responsible of a southward magnetic field directed as the dipole and with a magnitude of a few tens of nanoTeslas during quiet geomagnetic conditions and up to several tens of nanoTeslas under disturbed

conditions. Magnetopause currents contribute less to the measured magnetic field, the direction being as that of the ring current, but with an opposite orientation and with an estimated magnitude around 22 nT during quiet time and some tens of nanoTeslas during disturbed geomagnetic conditions (Maus and Lühr 2005). Consequently, the magnetopause current usually causes an enhancement of the geomagnetic field intensity. Typical time variations of ionospheric and magnetospheric contributions occur on scales from fractions of second to several hours, and their spatial scales range from a few kilometres to hundreds of kilometres.

In addition to these primary magnetospheric magnetic fields, also their induced counterparts should be considered. The external sources, besides their fast variations, exhibit variations on longer timescales due to their strong dependence on radiation and particles coming from the Sun during both quiet and active periods. For this reason external fields show also seasonal, annual and decadal variations. Even from a simplified picture of the problem, as that depicted above, it is clear that the task to separate all the contributions to the geomagnetic field is difficult considering the large variety of external sources that partially overlap each other on both temporal and spatial scales. The long distance effect of field-aligned currents and the Interplanetary Magnetic Field (IMF) penetration into the magnetosphere further complicates the picture. This penetration appears as a correlation between IMF B_y azimuthal component and observed magnetic field, and it could be present not only in regions characterised by open field lines, but also in those characterised by closed field lines (Cowley and Hughes 1983; Newell et al. 1995). More recently, this penetration has been observed in ground observatory and LEO (Low Earth Orbit) satellite magnetic data (Lesur et al. 2005).

Modelling the Earth's magnetic field

Among the outcomes of the high-precision measurements of the geomagnetic field, as those made by Swarm satellites, stands the increase of geomagnetic field models accuracy. Magnetic models can be grossly divided into two categories according to the way they approach to source separation. The first uses the comprehensive approach (Sabaka et al. 2004, 2015) consisting in modelling together the different sources. The other approach is to consider those observations less affected by external sources (night-time to minimise the ionospheric contribution and quiet magnetic conditions to minimise the magnetospheric one) to model the internal field. In this case the remaining external contributions are modelled considering the geometry of the current and geomagnetic indices. For instance, ring current shape is well modelled by a degree 1 spherical harmonics and its

intensity by either D_{st}^1 or $Sym-H^2$ indices (Wanliss and Showalter 2006). Both the approaches mentioned above do not allow a complete removal of the external contributions, due to their complexity, when modelling the internal field. This limits the accuracy achievable by a high-resolution modelling of the Earth's magnetic field with data from LEO satellites. A better understanding of what contributes to residuals estimated from modelled data and measurements is then very useful. For instance, Lesur et al. (2005) found a clear correlation between the azimuthal IMF B_y and night-time residuals of the eastward component (Y) of the geomagnetic field measured by both ground observatories and Ørsted satellite. Among the possible causes of this correlation, Lesur et al. (2005) proposed two explanations. One based on the interhemispheric currents flowing in the night-side ionosphere but propended for the second, i.e. of the direct leakage of the IMF B_y into the magnetosphere. This agrees with the finding that IMF contributes to magnetic satellite measurements with about 10 % of its B_x and 25 % of its B_y components (Maus and Lühr 2005; Lühr and Maus 2010). Differently from Lesur et al. (2005), in a study on the effect of IMF B_y on residuals of the Y component at low and mid-latitudes for a two-year period and all local times, Vennerstrom et al. (2007) found that the main source of IMF B_y and B_z (north–south component) perturbation on the Y component is the long distance effect of high-latitude FAC whose pattern depends on IMF direction. More recently, Kunagu et al. (2013) applied a continuous wavelet transform to mid-latitude CHAMP magnetic data focusing primarily on the 27-day periodicity they found in X , Y and Z residuals and in IMF B_y . This periodicity, present in geomagnetic components, is characterised by an intermittent temporal structure probably due to a LT dependency, and no LT dependency was found in IMF B_y . These findings support results found by Vennerstrom et al. (2007) and question those by Lesur et al. (2005).

This controversy has brought us to study the features of residuals in the Solar Magnetic (SM) frame when Swarm data are used. These residuals are estimated as the difference between satellite magnetic measurements and modelled data representing both internal and external magnetic fields. Precisely, we use low and mid-latitudes (between 50° S and 50° N SM latitude) data from Swarm satellites and CHAOS-5 model (Finlay et al. 2015), one of the most up-to-date magnetic models able to represent both internal (core and lithosphere) and external magnetic fields. We study the behaviour of calculated

residuals according to the polarities of IMF B_y and B_z and Dipole Local Time (DLT) to verify whether one of the hypotheses previously made on the possible relation between IMF B_y and Y component residuals can be confirmed with Swarm data. Then, we investigate the structure of residuals of the horizontal component H of the geomagnetic field as a function of $Sym-H$ index and DLT.

Data reprocessing is described in detail in the next section together with the method adopted to gain a deeper knowledge on the magnetic field mapped into analysed residuals. The “**Results and discussion**” part is devoted to the description of what emerges from the proposed analysis, and finally, in “**Conclusions**” results are interpreted and the main findings summarised.

Methods

Data reprocessing

In this study we use low-resolution (1 Hz) magnetic vector measurements taken on board the three Swarm satellites Alpha (A), Bravo (B) and Charlie (C). We analyse Level 1b magnetic data³ that according to ESA nomenclature are called SW_OPER_MAGx_LR_1B ($x = A, B, C$) with file counter equal to 0405, in particular measurements rotated in the NEC (North-East-Centre) frame. This version of Swarm vector data is corrected for a disturbance likely due to the position of the Sun with respect to Swarm satellites (details can be found in Lesur et al. 2015).

Selected data cover the time period between 1 March 2014 and 31 May 2015. During this period Swarm A and C have flown at an average altitude of ~470 km and Swarm B of ~520 km.

The procedure described in the following has been applied on data from Swarm A, B and C, separately. All the figures included in this paper refer to Swarm A only, and the same figures drawn with data from Swarm B and C are available as additional files.

Since the purpose of this work is to investigate the properties of unmodelled external contributions, the modelled magnetic fields originated from the core and from lithospheric and large-scale magnetospheric sources are removed from Swarm measurements. To achieve this, we subtract from each measurement a value obtained using CHAOS-5 (Finlay et al. 2015) model that takes into account these contributions. This value is estimated at the same location (latitude, longitude and altitude) and at the same time of Swarm measurement. In CHAOS-5, spherical harmonics degrees from 1 to 90 represent the internal field, and those from 1 to 20 the core field temporal variations. Spherical harmonics expansion is then made in SM coordinates up to degree 2

¹ Information is available at <http://wdc.kugi.kyoto-u.ac.jp/dstdir/>.

² A report explaining the derivation of $Sym-H$ can be found at wdc.kugi.kyoto-u.ac.jp/aeasy/asy.pdf.

³ Available at <ftp://swarm-diss.esa.int> upon registration.

for the ring current, in Geocentric Solar Magnetospheric (GSM) coordinates up to degree 2 and order 0 for magnetopause and magnetotail currents (Olsen et al. 2014). We use CHAOS-5_v4 based on Swarm Level 1b and ground observatory data as available in June 2015 and able to model the external field until 6 June 2015. Detailed information on CHAOS-5 (documentation and code) is freely available.⁴

After removal of CHAOS-5 values from Swarm measurements, residuals are corrected for spikes (generally due to brief periods of switched off vector magnetometer) and rotated from the NEC frame into the SM frame to have a better point of view of solar wind influence on examined residuals (Maus and Lühr 2005). SM frame is Earth-centred with z -axis parallel to the magnetic dipole and positive northward, y -axis perpendicular to the Earth–Sun line and positive duskward and x -axis completing the right-handed system (Kivelson and Russell 1995). In this system, spherical coordinates are identical to a dipole-colatitude system. Therefore, the use of Dipole Local Time, which is defined relative to the dipole system, is preferable to that of Magnetic Local Time that is defined with respect to a non-orthogonal coordinate system (more details in Olsen et al. 2007, pp. 37–38).

We firstly estimate residuals of the Y and H components (dY and dH) at SM latitudes between 50° S and 50° N. Residuals at higher SM latitudes deserve a separate treatment due to the more complicate contributing current systems (e.g. polar cap ionospheric currents, auroral electrojets and field-aligned currents)—not discussed in this work. For each satellite, the obtained residuals are then separated into different subsets based on: the polarity of IMF B_y and B_z components (in GSM coordinates) as concerns dY and on the value of the geomagnetic activity index $Sym-H$ as concerns dH . The choice to investigate the dependence of dY residuals on IMF B_y separately for IMF B_z different polarities relates to the very different large-scale dynamics and morphology that characterise the magnetosphere when IMF switches from southward to northward. The choice to investigate dH residuals for different values of $Sym-H$ index has two purposes: to study the dependence of residuals on the level of geomagnetic disturbance actually observed on the ground independently of solar conditions and to focus on the possible unmodelled magnetic field linked to the ring current.

Taking into account the different polarities of IMF B_y and B_z we define four different sectors: sector I ($B_y > 0$; $B_z > 0$), sector II ($B_y < 0$; $B_z > 0$), sector III ($B_y < 0$; $B_z < 0$) and sector IV ($B_y > 0$; $B_z < 0$). Concerning $Sym-H$ we

define two different geomagnetic conditions: quiet when $|Sym-H| \leq 5$ nT and disturbed when $|Sym-H| \geq 20$ nT. Residuals resulting from the separation into IMF sectors and into quiet and disturbed conditions are mapped in Figs. 1 and 2.

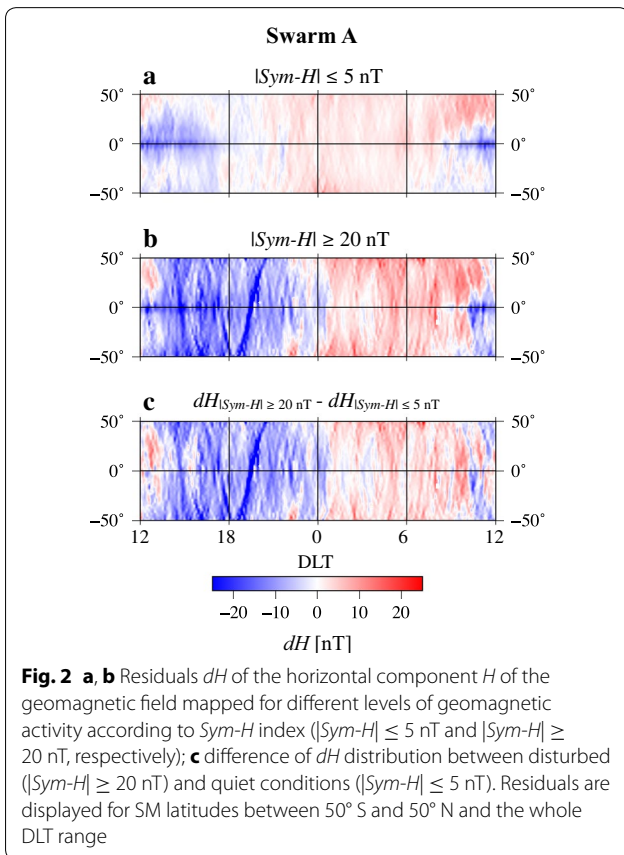
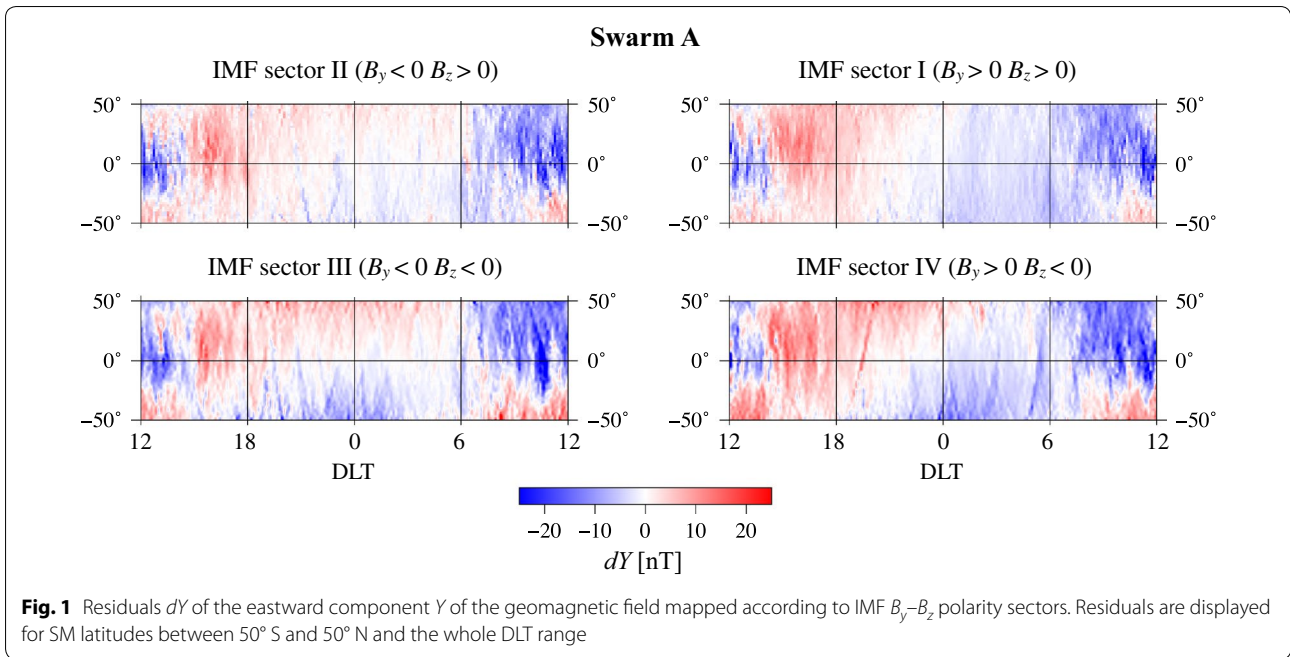
To draw Figs. 1 and 2, Swarm A residuals from each subset are grouped according to their SM latitude and longitude into $2^\circ \times 2^\circ$ bins, mapped values consisting of the averages of the values of dY and dH residuals, respectively, falling in each bin.

On average, each bin is populated with around 500 values. As far as concerns Figs. 1 and 2a no empty bin is found, while concerning Fig. 2b, c a small number of bins (less than 1 % of the total number) result to be empty. The same applies to the analogous figures drawn for Swarm B and C (Additional files 1, 2, 3, 4).

From Fig. 1, showing the DLT distribution of dY residuals depending on the IMF sector, the main visible difference in the structure of dY is between sectors with $B_y > 0$ (I–IV) and those with $B_y < 0$ (II–III). In sectors I and IV, positive (red) residuals prevail in the dusk-side, while negative (blue) in the dawn-side. Differently, in sectors II and III positive and negative residuals are dominant around midnight and noon, respectively, above the equator. Below the equator the configuration is the opposite. Average absolute amplitudes are little higher in sectors with $B_z < 0$ (III and IV) than in sectors with $B_z > 0$ (I and II). In Fig. 1 it is not possible to recognise univocally a current system responsible of the observed pattern. The disturbance observed at mid-latitudes on the Y component can be mainly ascribed to FAC (Sun et al. 1984); however, the ionospheric contribution, especially during daytime, can play an important role. The situation is different at night-time when, due to the low conductivity of the ionosphere, it is possible to attribute perturbations observed on the Y component mainly to the magnetospheric sources. Besides the solar quiet current system contribution, also that produced at low latitudes by the interhemispheric field-aligned currents could be mapped into dY residuals. A recent study shows that this contribution maximises at around 18 MLT and 12 MLT (Lühr et al. 2015). Since these currents have an orientation that is opposite over the summer and winter periods, we consider their contribution negligible due to the average over 15 months.

Figure 2 shows the DLT distribution of dH residuals depending on different geomagnetic activity levels as measured by $Sym-H$ index. For quiet conditions ($|Sym-H| \leq 5$ nT, Fig. 2a), residuals tend to be generally positive however with small values. For disturbed conditions ($|Sym-H| \geq 20$ nT, Fig. 2b) the same general behaviour is seen but with an extension of the region of negative residuals and with overall higher absolute values. To

⁴ <http://www.spacecenter.dk/files/magnetic-models/CHAOS-5/>.

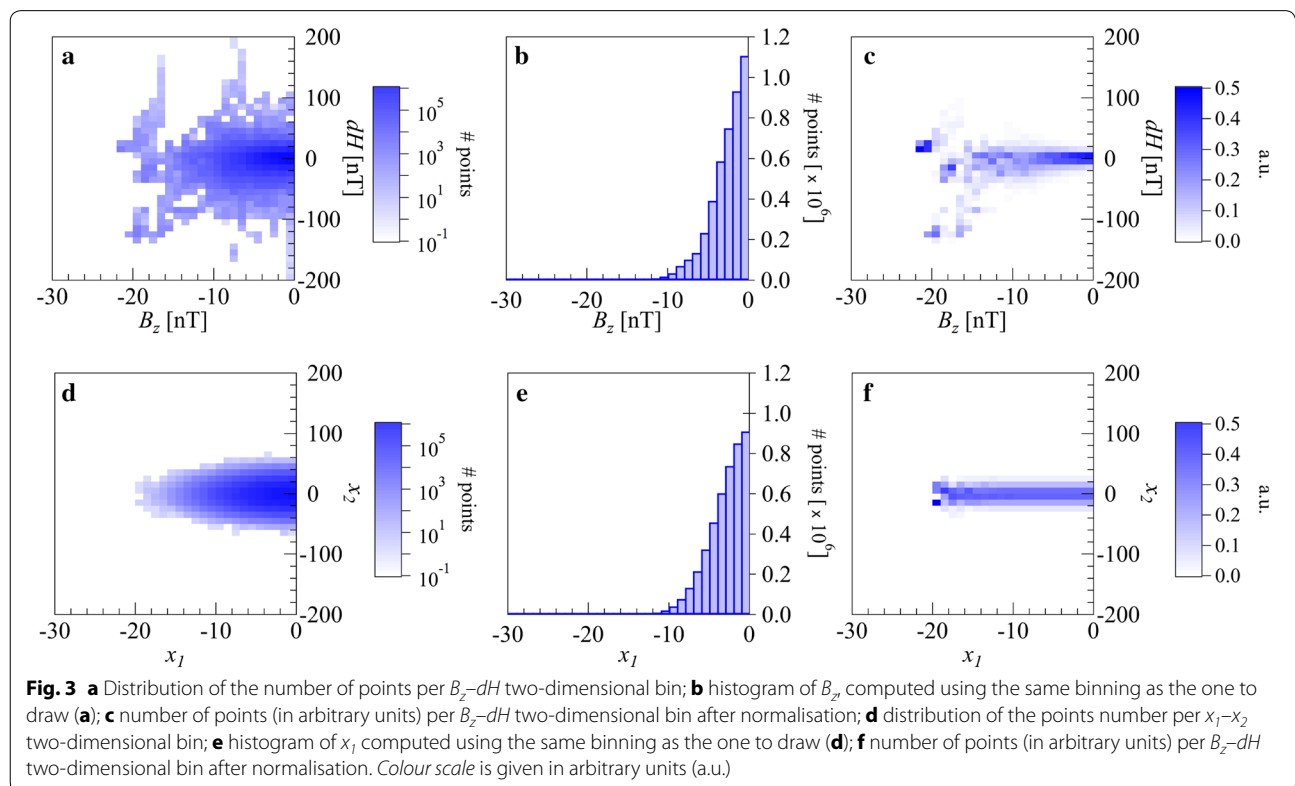


better visualise the difference between the distributions of dH under the two different conditions of geomagnetic activity we remove quiet dH residuals from disturbed ones to eliminate common features, particularly the quiet daytime ionospheric contribution. This contribution is evident in Fig. 2a, b in the 9–18 DLT interval when along the equator an intense band of negative residuals, wide about 20° in SM latitude, is present. It is clearly the signature on dH of the equatorial electrojet that appears as a negative contribution to the measured magnetic field at satellite altitude. What remains in Fig. 2c is mainly of magnetospheric origin. This is also supported by other authors (e.g. Langel and Sweeney 1971; Iyemori 1990; Yamashita et al. 2002) who found that residuals of Y and H components observed at the surface and at satellite altitude show a deflection in the same sense, thus implying that the source current is not in the ionosphere. The blue area of Fig. 2c at low and mid-latitudes in the 12–24 DLT interval suggests the existence of an equatorial electric current characterised by a dawn–dusk asymmetry acting almost uniformly over all the low- and mid-latitude range. A good candidate for such a current is the asymmetric part of the ring current, namely the partial ring current, that flows westward far from both the satellites, thus causing an asymmetric decrease in the horizontal component of the geomagnetic field (De Michelis et al. 1999).

An approach to investigate residuals dependency

To gain more information than that displayed in Figs. 1 and 2 we verify qualitatively the possible dependence of magnetic field residuals on both the polarity of IMF B_y and B_z and geomagnetic activity level. Concerning the dependence on IMF, at this stage we extend our study to all geomagnetic field components (dX , dY , dZ) in SM coordinates. A standard way to estimate the relation in terms of correlation coefficient between two time series is through the following steps: (1) subtract from each series its average, (2) divide each series by its standard deviation, (3) plot one series versus the other and (4) estimate the linear correlation coefficient that is given by the best line that fits the obtained scatter plot (Brandt 1970). The application of this method to data here considered is not straightforward due to the huge amount of points. Scatter plots of residuals as a function of one among IMF B_z , IMF B_y or $Sym-H$ would end in a cloud of points overlapping each other and hiding the existence of any possible correlation. We use a modified version of this approach that is capable of giving us a qualitative information on correlation. As an example, let us verify the existence of a possible relation between dH residuals and IMF southward B_z . To overcome the “cloud effect” we firstly bin the observations as in a two-dimensional histogram to display the distribution of values in a data set across the

range of two variables, IMF B_z and dH . After setting the width of the bins into which IMF B_z and dH are classified (1 nT for B_z and of 10 nT for dH), we count the number of points falling in each bin. This operation corresponds to estimating the elements a_{ij} ($i = 1, \dots, n$; $j = 1, \dots, m$) of a matrix A with number of rows n equal to the number of dH bins and a number of columns m corresponding to the number of B_z bins. We then display the values of a_{ij} (i.e. the count of observations in the data set within each two-dimensional dH - B_z bin) in Fig. 3a where, coherently with the definition of matrix A, B_z is placed on the abscissa (columns of matrix A) and dH on the ordinate (rows of matrix A). Since we consider a specific time window (1 March 2014–31 May 2015) mainly characterised by quiet and little disturbed conditions, we obtain a cloud of points. The bulk of observations corresponds to values of both B_z and dH around zero, and any possible relation between dH and B_z associated with moderate and highly disturbed geomagnetic conditions is hidden. To investigate the relation between B_z and dH when they are far from zero, we normalise the values of a_{ij} shown in Fig. 3a. In detail, once computed B_z histogram using the same bin width used to obtain Fig. 3a, we associate its values to a vector with elements h_j ($j = 1, \dots, m$). Matrix A is then transformed into a new matrix B with elements defined as $b_{ij} = a_{ij}/h_j$ ($i = 1, \dots, n$; $j = 1, \dots, m$) and



displayed graphically in Fig. 3c. This operation allows to flatten structures due to highly populated B_z bins and to enhance those due to poorly populated B_z bins as shown in Fig. 3c that illustrates a structure also seen in Fig. 2a however not well noticeable.

To test our approach in the case of two independent Gaussian signals, we applied the same working steps to obtain Fig. 3a–c, based on two synthetic signals. These synthetic series, x_1 and x_2 , have the same lengths of B_z and dH , respectively. Moreover, x_1 and x_2 have been generated so as to follow each a Gaussian distribution with a mean and a standard deviation alike those of B_z and dH , respectively. Obtained results are shown in Fig. 3d–f. In Fig. 3f we observe a completely flat distribution meaning the independence of x_1 and x_2 . This agrees with the way x_1 and x_2 were generated, i.e. as two Gaussian independent time series.

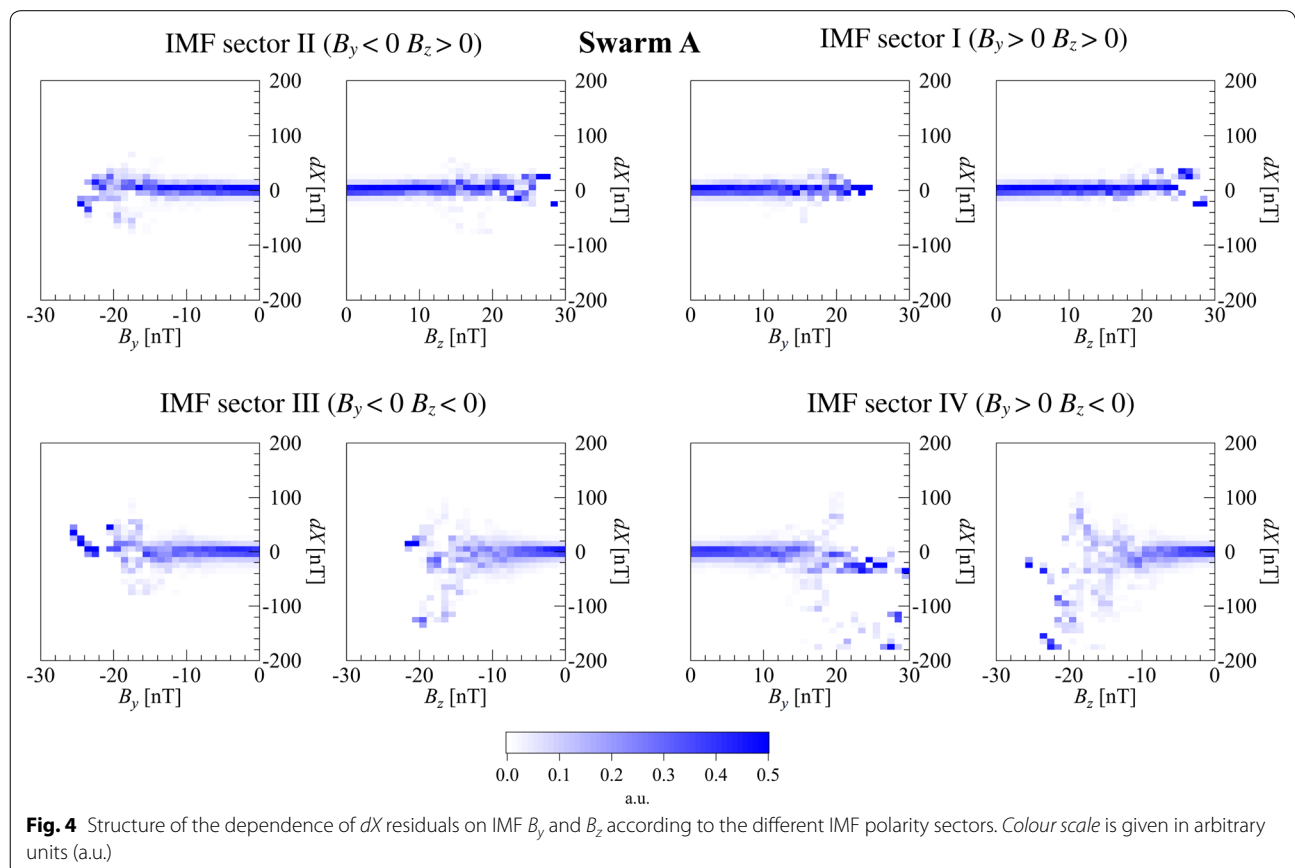
We apply this procedure to the four subsets corresponding to the different IMF sectors to investigate the qualitative correlation between dX , dY and dZ and IMF B_y and B_z and between dH and $Sym-H$ for different DLT ranges. Analogously to the bin widths used in the example illustrated above, we consider a bin width of 1 nT for B_y and B_z and of 10 nT for $Sym-H$ and magnetic residuals.

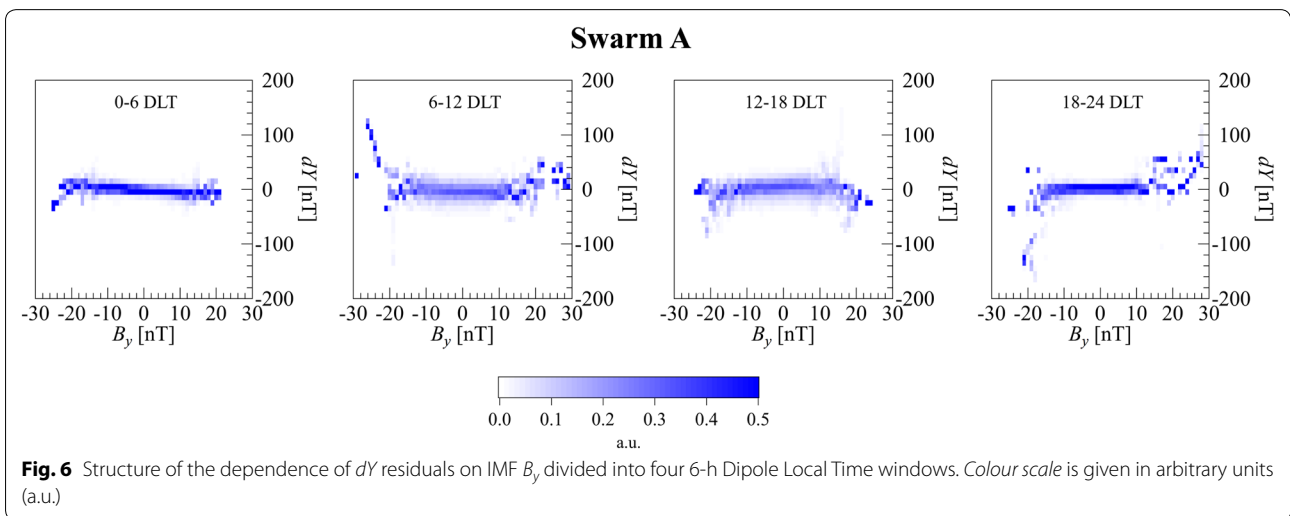
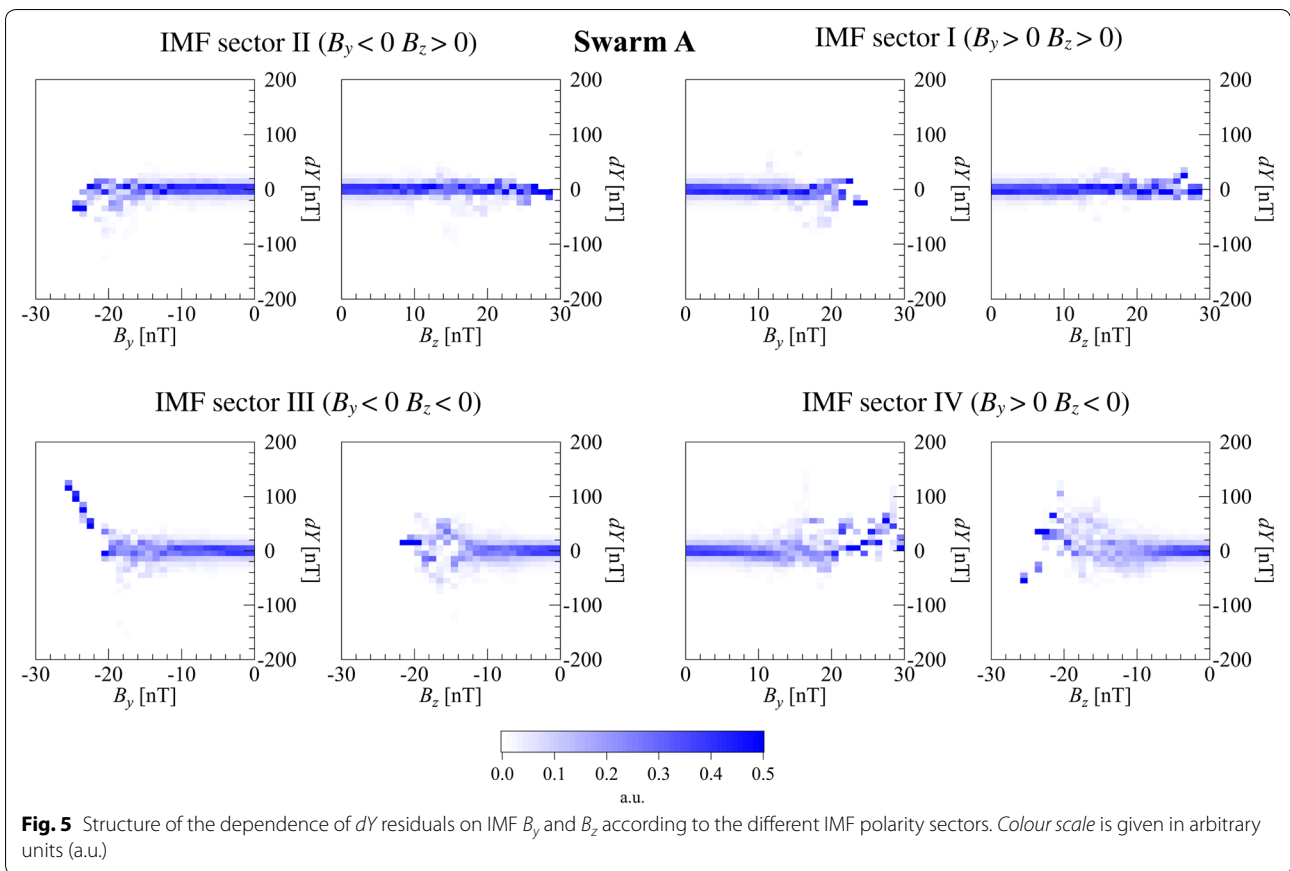
The value of the bin width is a compromise between a sufficient number of points in each bin and the resolution of the image representing the structure between residuals and B_y , B_z and $Sym-H$. Results for Swarm A are shown in Figs. 4, 5, 6, 8 and 9 and discussed in the following section (results related to Swarm B and C are displayed in the figures corresponding to Additional files 5, 6, 7, 8, 9, 10, 11, 12, 13, 14).

Results and discussion

Part I: dependence on B_y and B_z

Figures 4 and 5 display the structures of the dependence of dX and dY on IMF sector obtained applying the method explained in the previous section. Starting from sector I we observe a practically flat behaviour (at that of Fig. 3f) for both geomagnetic components, indicating the lack of any relation between dX and dY residuals and B_y or B_z . Moving to sectors III and IV, Figs. 4 and 5 show a clear dependence of dX and dY on B_z , i.e. dX and dY residuals become larger and larger (in absolute value) with decreasing B_z . The predominant sign of dX residuals is negative with amplitudes larger than that of dY . The observed behaviour of dX with B_z could be the result of the ring current that generates a southward





magnetic field oriented along the dipole. It is well known that the direction of IMF B_z component controls the growth and decay of the ring current; indeed, it is possible to build models able to reconstruct the growth of ring current intensity giving as input only the values of the interplanetary electric field in the ecliptic

plane normal to the Sun–Earth line (Burton et al. 1975; Kamide et al. 1998).

Interestingly, in these sectors we also observe a dependence on B_y . In sectors III and IV, the amplitudes of dX and dY increase (in absolute value) with the decrease (sector III) and the increase (sector IV) of B_y . Considering these

two sectors alone, it is not possible to assess the dependence of dX and dY residuals on B_y , since in both cases the increase (in absolute value) of the amplitude of dX and dY residuals could be ascribed to the negative B_z . An elucidating result is contained in sector II where B_z is positive: even if less marked than in sectors III and IV, the absolute values of dX and dY residuals tend to increase when B_y becomes more and more negative, while they seem to be independent of B_z . When performed on dZ residuals, the same investigation displays a flat behaviour in IMF sectors I, II and III, while in sector IV dZ residuals tend to moderately increase with the absolute value of B_y and B_z (Additional files 15, 16, 17).

To further study the dependence of dY residuals on IMF B_y , residuals are grouped according to 6-h DLT intervals. The resulting distribution is shown in Fig. 6. In the case of a direct penetration of IMF B_y , we would expect it to be anti-correlated with dY on the night-side and positively correlated on the day-side. Due to the possible effects of the ionosphere on the day-side we focus on the night-side. Here, the DLT interval worth being noticed is the 18–24 one where dY and B_y appear to be positively correlated for values of $|B_y| > \sim 15$ nT. This behaviour agrees with Vennerstrom et al. (2007) finding of a positive correlation between the Y component measured at three magnetic observatories and IMF B_y in the interval 12–24 MLT (Magnetic Local Time).

The presented analysis underlines the dependence of dX and dY residuals on B_y , but due to the width of the bin used for magnetic residuals (10 nT) we are not able to solve definitively the controversy between those supporting the hypothesis of a direct penetration and those supporting that of the long-range effect of field-aligned currents. In fact, the amplitude of the penetrating IMF B_y is of a few nanoTeslas, generally less than 10 nT (the resolution of Figs. 4, 5, 6, 7, 8, 9). However, the positive correlation found for the 18–24 DLT interval makes us propend for the hypothesis of a long-range influence of high-latitude FAC.

To further sustain these conclusions and visualise the pattern of the perturbation associated with each polarity of B_z and B_y , we evaluate the differences between dY residuals corresponding to the different polarities of B_z and B_y and show them in Fig. 7 (the analogous figures for Swarm B and C are in the Additional files 18, 19). Figure 7 displays: a) the difference between residuals corresponding to $B_z < 0$ and those with $B_z > 0$ regardless of B_y orientation, b) the difference between residuals corresponding to $B_y > 0$ and those with $B_y < 0$ regardless of B_z orientation. The mapped differences are consistent with what presented by Vennerstrom et al. (2007) who have computed both the perturbation due to statistical FAC patterns derived from Papitashvili et al. (2002) and

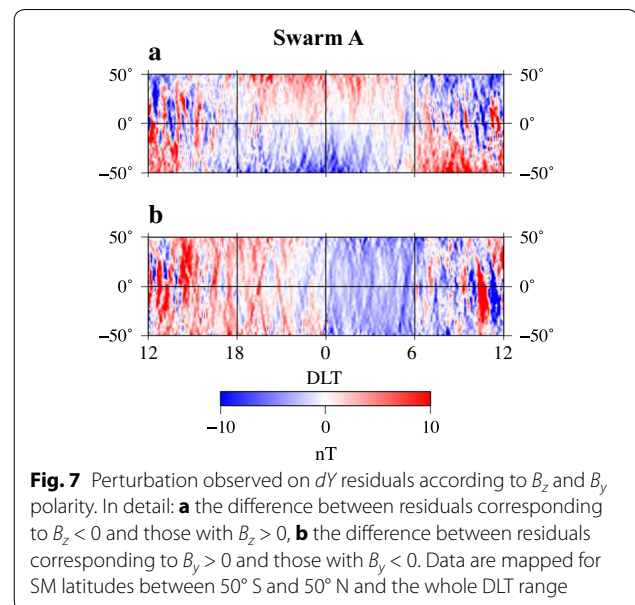
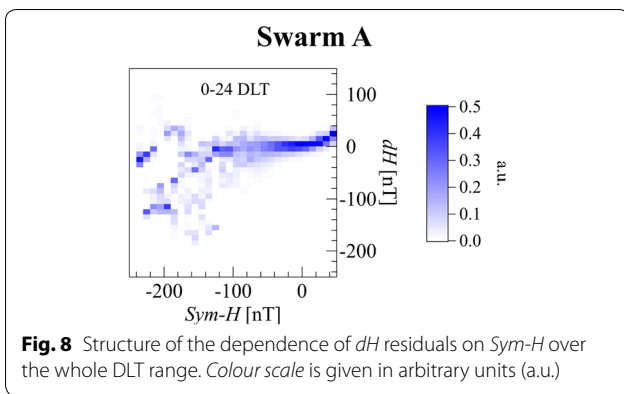


Fig. 7 Perturbation observed on dY residuals according to B_z and B_y polarity. In detail: **a** the difference between residuals corresponding to $B_z < 0$ and those with $B_z > 0$, **b** the difference between residuals corresponding to $B_y > 0$ and those with $B_y < 0$. Data are mapped for SM latitudes between 50° S and 50° N and the whole DLT range

the observed average perturbation obtained with Ørsted data. Our Fig. 7a, b well agrees with their Figs. 3a, c, d and 4c, d, respectively. In accordance with the statistical FAC pattern they calculated, but in disagreement with their observations, we find similar intensities of the perturbation in the northern and the southern hemispheres.

However, other currents could explain the perturbation observed on Y component reported in Fig. 7a as well as that observed on the H component (Fig. 2c), i.e. the net field-aligned currents resulting from unbalanced Region 1 and Region 2 currents. These have been theoretically hypothesised by Crooker and Siscoe (1981) and by Chen et al. (1982) to explain the dawn–dusk asymmetry of the disturbance observed in the north–south geomagnetic component and the features of the disturbance observed in the east–west component at low and mid-latitudes. Evidences of net field-aligned currents have been discovered later in satellite observations (e.g. Yamashita et al. 2002; Nakano and Iyemori 2003). According to Crooker and Siscoe (1981) they are expected to flow into the ionosphere on the day-side and out of the ionosphere on the night-side. Using data from DE-1 satellite (Farthing et al. 1981), Nakano and Iyemori (2003) found that net downward and upward currents reach their maximum intensity in the 6–12 MLT and 18–24 MLT intervals, respectively, while they are characterised by a small intensity in the remaining MLTs. After the estimation of these currents across the entire MLT range, Nakano and Iyemori (2003) also estimated the magnetic effect that they are expected to produce at 30° in dipole latitude on Y and H components. Results (shown in their Fig. 8) closely match our findings reported in Figs. 2c and 7a.

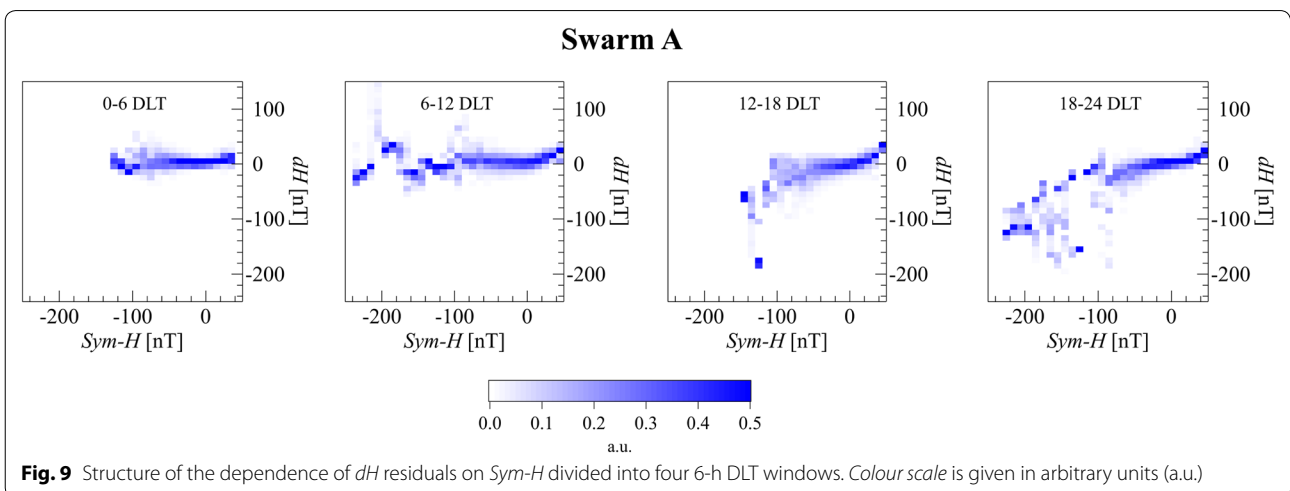


Net field-aligned currents are associated with periods of strongly negative IMF B_z and hence to periods characterised by geomagnetic storms. The effect modelled at mid-latitudes on the horizontal component H is characterised by a clear dawn–dusk asymmetry, with negative perturbation on the dawn-side and positive on the dusk-side (as in our Fig. 2c). The effect on Y component is negative in the 6–18 MLT interval and positive in the 0–6 and 18–24 MLT intervals (as in our Fig. 7a). As concerns Y component the effect is reversed in the southern Hemisphere.

Part II: dependence on $Sym-H$

Turning now to the experimental evidence of the relation between dH and $Sym-H$ reported in Fig. 2, we apply, also in this case, our approach for residuals dependency. Figure 8 shows variations of dH as a function of $Sym-H$ over the whole 0–24 DLT range. For $Sym-H$ larger than about -60 nT we observe an almost flat behaviour, while for smaller values two distinct branches appear, indicating the existence of a dependence. A possible explanation of the nature of the branch corresponding to negative

dH might be given in terms of ring current growth. The presence of this contribution manifests also in the striking dependence of dX on negative B_z values (Fig. 4). The branch corresponding to positive dH is more difficult to interpret (see further discussion). In order to go deeper with an understanding for this behaviour, we divide data used in Fig. 8 into 6-h intervals (0–6, 6–12, 12–18 and 18–24 DLT) and show the corresponding distributions in Fig. 9. The first two time sectors (0–6 and 6–12) show an almost flat behaviour of dH as a function of $Sym-H$. The only exception is a feature appearing in the 6–12 DLT interval for $Sym-H$ around -200 nT similar to the positive branch of Fig. 8. Searching the values of dH responsible for this feature we find that they correspond to observations made around 20 LT and 23:30 UT of 17 March 2015, i.e. during the so-called St. Patrick storm, the most intense storm of the present solar cycle. These observations present an anomaly, i.e. to very low $Sym-H$ values, indicating a sustained ring current, large positive dH values exist instead of the largely negative expected. Due to the value of local time, this anomaly cannot be ascribed to some ionospheric effect but to some measurement errors during the peak of the storm or in an overestimated ring current intensity in this DLT interval by CHAOS-5. In the 12–18 DLT interval, dH shows a decrease with decreasing $Sym-H$ that becomes more intense in the next interval (18–24 DLT). The evolution of the behaviour in the four DLT intervals could be imputed to the effect of a westward electric current characterised by an intensity peaking in the dusk-side. This is the partial ring current located in the dusk sector, reaching its peak in 18–20 MLT (Liemohn et al. 2001; Li et al. 2011) and closing through field-aligned currents into the ionosphere. During magnetic storms, particles are injected in the inner magnetosphere from the tail and



intensify the ring current around midnight. Then ions begin to drift westward, and, especially during intense storms, part of them is lost through the day-side magnetopause (Liemohn et al. 1999).

At this point we call the reader attention on the 0–6 DLT interval where no observation corresponds to $Sym-H < -130$ nT. Comparing the behaviour in this interval with those in the other intervals we notice that when a significant decrease of dH occurs it starts at values of $Sym-H$ around $-80 \div -60$ nT, we then could expect that the flat behaviour observed between -130 and -80 nT continues also for smaller $Sym-H$ values. Therefore, the absence of negative values of dH between 0 and 12 DLT would be indicative of ring current weakening in this DLT interval. So far we focused on contributions of magnetospheric origin. Looking at the range of values covered by dH residuals in the 6–12 and 12–18 DLT intervals for $Sym-H$ higher than around -25 nT, we observe that here this range is wider than in sectors 0–6 and 18–24 DLT. This can be interpreted as the quiet day-side signature of the ionospheric contribution, also visible in Fig. 2a, b.

Conclusions

In this study we have regarded to the dependence of geomagnetic field residuals, in the SM frame, on IMF B_y and B_z components and on $Sym-H$ index to try to unveil the nature of unmodelled contributions in geomagnetic field models.

Concerning the dependence on IMF components, we have found a correlation between residuals of the X and Y component of the geomagnetic field and B_y , regardless of B_z orientation. This correlation is positive in the 18–24 DLT interval.

Analysing the distribution of the perturbation mapped in dY residuals for different polarities of B_z and B_y we have found a result remarkably similar to that obtained by Vennerstrom et al. (2007), which has been interpreted as the effect of FAC at low- and mid-latitudes. Indeed, although at low- and mid-latitudes FAC are very far from the Earth (several Earth radii), their magnetic effect is well measurable as confirmed by Kunagu et al. (2013). Our findings seem to suggest the presence of FAC's magnetic contribution on the obtained residuals which are characterised by an average amplitude around 3 nT as obtained averaging over all SM latitudes and all DLTs the absolute value of the perturbation on the Y component shown in Fig. 7. Due to the morphology of dY residuals in the different IMF sectors (Fig. 1) the effect of IMF B_y seems to be responsible of a change in the direction of FAC. For $B_y > 0$ we find positive and negative dY residuals approximately arranged into separate vertical DLT bands, while for $B_y < 0$ these bands are no more vertical but inclined (positive residuals

expanding downward in the northern hemisphere and negative residuals moving duskward in the southern hemisphere).

The penetration of IMF B_y into the magnetosphere cannot be confirmed by the proposed analysis, due to a resolution problem of Figs. 4, 5 and 6. Taking into account that the fraction of penetrating IMF B_y is estimated to be 25 % of its amplitude (Maus and Lühr 2005), since the absolute value of B_y is less than 8 nT for 95 % of the considered data set and its average is around 3 nT, the average (over all SM latitudes and all DLTs) perturbation on the Y component can be estimated to be less than 1 nT. Of course if we consider peaks of B_y magnitude, the penetrating IMF B_y can reach values of the order of 10 nT; however, this happens in restricted time intervals. Therefore, we cannot exclude that, in our case, the more intense and spread FAC effect overwhelms that of the temporally more localised B_y leakage. Let us finally recall that some empirical magnetospheric models include the phenomenon of IMF penetration (Tsyganenko 2013). Concerning the relation of dH residuals and $Sym-H$ index we have found that residuals seem to be strongly affected by the effect of the partial ring current in accordance with previous results (e.g. Langel and Sweeney 1971). In Fig. 2c the effect on dH residuals due to the quiet ionosphere is removed, and only measurements taken under geomagnetically disturbed conditions are considered. During high levels of geomagnetic activity the combined effects of different large-scale magnetospheric currents such as the magnetopause current, the cross-tail current, the ring current and partial ring current are recorded. These current systems have different origin, topology and effect on the geomagnetic field. The magnetopause current produces an increase of the geomagnetic field; the cross-tail current at the night sector causes a weak day–night asymmetric depression on the horizontal component of the geomagnetic field; and the symmetric ring current causes an almost identical depression of the same component for all magnetic local times. Thus, the significant dawn–dusk asymmetry observed in the spatial–temporal distribution of dH residuals can be reasonably attributed to the partial ring current located in the dusk sector peaking around 18–20 DLT (Li et al. 2011). Different estimations of the partial ring current contribution to the observed D_{st} have been given. Turner et al. (2001) found a contribution around 75 % for small and moderate storms ($-100 \text{ nT} \leq Sym-H \leq -50 \text{ nT}$) and around 40 % for intense storms ($-250 \text{ nT} \leq Sym-H \leq -100 \text{ nT}$), while Li et al. (2011) found 87 % for moderate storms and 58 % for intense storms. Results shown in Figs. 8 and 9 suggest that the used model

well represents the ring current contribution for $Sym-H > -80$ nT, underestimating it for higher $Sym-H$. These results suggest that CHAOS-5 well models symmetric ring current. Nevertheless, the CHAOS-5 model does not consider that during the main phase and early recovery phase of a magnetic storm the contributing current is strongly asymmetric due to either the loss of ions through the day-side magnetopause and the activation of a dusk-centred partial ring current. This asymmetry is lost in the later recovery phase. On the basis of the results shown in Fig. 2c we can also provide a qualitative estimation of average perturbation due to this asymmetric current during the development of mainly small and moderate geomagnetic storms that have occurred in the analysed period. On the whole period from 1 March 2014 to 31 May 2015 the average value of the perturbation due to the asymmetric ring current is of -5 nT, while during the St. Patrick storm, i.e. the vertical signature in Fig. 2c around 19 DLT, is of about -30 nT. Considering that the contribution due to the ring current ranges between a few tens to several hundreds of nanoTeslas (from quiet to disturbed period), the average unmodelled contribution is quite low. Another possible interpretation of the features observed on Swarm dY and dH residuals is given in terms of the magnetic effect at low and mid-latitudes of net field-aligned currents flowing into the ionosphere on the day-side and out of the ionosphere on the night-side as theoretically hypothesised by Crooker and Siscoe (1981). However, considering the length of available used data (15 months), and the difficulties in magnetic source separation, we have to stress that the identification of the sources of the observed residuals is not univocal.

Nevertheless, the results of this study indicate that the simultaneous use of Swarm data and CHAOS-5 model provides the opportunity to improve geomagnetic field models including effects of current systems that, so far, have not been considered. This study is a very first attempt to characterise unmodelled contributions in satellite-based models using data from the three Swarm satellites and CHAOS-5 on a 15-month time window. A more detailed analysis of the dependence of geomagnetic residuals on IMF and geomagnetic indices could certainly take advantage of data over a longer time interval therefore allowing the investigation of the seasonal dependence, important especially concerning the FAC variability and the possible contribution of interhemispheric field-aligned currents, and also the semiannual variation in geomagnetic activity through the Russell–McPherron effect (Russell and McPherron 1973).

Additional files

Additional file 1: Figure B1. Swarm B residuals dY of the Eastward component Y of the geomagnetic field mapped according to IMF B_y – B_z polarity sectors. Residuals are displayed for SM latitudes between 50° S and 50° N and the whole DLT range.

Additional file 2: Figure C1. Swarm C residuals dY of the Eastward component Y of the geomagnetic field mapped according to IMF B_y – B_z polarity sectors. Residuals are displayed for SM latitudes between 50° S and 50° N and the whole DLT range.

Additional file 3: Figure B2. a and b Swarm B residuals dH of the horizontal component H of the geomagnetic field mapped for different levels of geomagnetic activity according to $Sym-H$ index ($|Sym-H| \leq 5$ nT and $|Sym-H| \geq 20$ nT, respectively); **c** difference of dH distribution between disturbed ($|Sym-H| \geq 20$ nT) and quiet conditions ($|Sym-H| \leq 5$ nT). Residuals are displayed for SM latitudes between 50° S and 50° N and the whole DLT range.

Additional file 4: Figure C2. a and b Swarm C residuals dH of the horizontal component H of the geomagnetic field mapped for different levels of geomagnetic activity according to $Sym-H$ index ($|Sym-H| \leq 5$ nT and $|Sym-H| \geq 20$ nT, respectively); **c** difference of dH distribution between disturbed ($|Sym-H| \geq 20$ nT) and quiet conditions ($|Sym-H| \leq 5$ nT). Residuals are displayed for SM latitudes between 50° S and 50° N and the whole DLT range.

Additional file 5: Figure B4. Structure of the dependence of Swarm B dX residuals on IMF B_y and B_z according to the different IMF polarity sectors. Colour scale is given in arbitrary units (a.u.).

Additional file 6: Figure C4. Structure of the dependence of Swarm C dX residuals on IMF B_y and B_z according to the different IMF polarity sectors. Colour scale is given in arbitrary units (a.u.).

Additional file 7: Figure B5. Structure of the dependence of Swarm B dY residuals on IMF B_y and B_z according to the different IMF polarity sectors. Colour scale is given in arbitrary units (a.u.).

Additional file 8: Figure C5. Structure of the dependence of Swarm C dY residuals on IMF B_y and B_z according to the different IMF polarity sectors. Colour scale is given in arbitrary units (a.u.).

Additional file 9: Figure B6. Structure of the dependence of Swarm B dY residuals on IMF B_y divided into four 6-h Dipole Local Time windows. Colour scale is given in arbitrary units (a.u.).

Additional file 10: Figure C6. Structure of the dependence of Swarm C dY residuals on IMF B_y divided into four 6-h Dipole Local Time windows. Colour scale is given in arbitrary units (a.u.).

Additional file 11: Figure B8. Structure of the dependence of Swarm B dH residuals on $Sym-H$ over the whole DLT range. Colour scale is given in arbitrary units (a.u.).

Additional file 12: Figure C8. Structure of the dependence of Swarm C dH residuals on $Sym-H$ over the whole DLT range. Colour scale is given in arbitrary units (a.u.).

Additional file 13: Figure B9. Structure of the dependence of Swarm B dH residuals on $Sym-H$ divided into four 6-h DLT windows. Colour scale is given in arbitrary units (a.u.).

Additional file 14: Figure C9. Structure of the dependence of Swarm C dH residuals on $Sym-H$ divided into four 6-h DLT windows. Colour scale is given in arbitrary units (a.u.).

Additional file 15: Figure A10. Structure of the dependence of Swarm A dZ residuals on IMF B_y and B_z according to the different IMF polarity sectors. Colour scale is given in arbitrary units (a.u.).

Additional file 16: Figure B10. Structure of the dependence of Swarm B dZ residuals on IMF B_y and B_z according to the different IMF polarity sectors. Colour scale is given in arbitrary units (a.u.).

Additional file 17: Figure C10. Structure of the dependence of Swarm C dZ residuals on IMF B_y and B_z according to the different IMF polarity sectors. Colour scale is given in arbitrary units (a.u.).

Additional file 18: Figure B7. Perturbation observed on Swarm B dY residuals according to B_z and B_y polarity. In detail: **a** the difference between residuals corresponding to $B_z < 0$ and those with $B_z > 0$, **b** the difference between residuals corresponding to $B_y > 0$ and those with $B_y < 0$. Data are mapped for SM latitudes between 50° S and 50° N and the whole DLT range.

Additional file 19: Figure C7. Perturbation observed on Swarm C dY residuals according to B_z and B_y polarity. In detail: **a** the difference between residuals corresponding to $B_z < 0$ and those with $B_z > 0$, **b** the difference between residuals corresponding to $B_y > 0$ and those with $B_y < 0$. Data are mapped for SM latitudes between 50° S and 50° N and the whole DLT range.

Abbreviations

CHAMP: Challenging Minisatellite Payload; ESA: European Space Agency; VFM: Vector Field Magnetometer; STR: Star Trackers; CSC: Compact Spherical Coil; ASM: Absolute Scalar Magnetometer; CHU: Camera Head Unit; FAC: field-aligned currents; IMF: Interplanetary Magnetic Field; LEO: Low Earth Orbit; LT: Local Time; SM: Solar Magnetic; DLT: Dipole Local Time; NEC: North-East-Centre; GSM: Geocentric Solar Magnetospheric; MLT: Magnetic Local Time; UT: Universal Time.

Authors' contributions

RT designed the study on an idea by MM, developed the methodology, performed the analysis and drafted the manuscript. MM and PDM participated in designing the study, in the interpretation of results and in constructing the manuscript. All authors read and approved the final manuscript.

Author details

¹ Istituto Nazionale di Geofisica e Vulcanologia, Via di Vigna Murata 605, 00143 Rome, Italy. ² CNES - Centre National d'Etudes Spatiales, Paris, France.

Acknowledgements

We thank all members of the ESA Swarm team for their precious work, which is the basis for our investigations. Magnetic data used here are the Swarm Level 1b MAGA_LR freely accessible at <https://earth.esa.int/web/guest/swarm/data-access>. We acknowledge use of NASA/GSFC's Space Physics Data Facility's CDAWeb service, and OMNI data, geomagnetic indices and OMNI IMF data were obtained at <http://cdaweb.gsfc.nasa.gov/>. We are also grateful to the authors of CHAOS-5 for making their model available. Figures 1, 2 and 7, B1, B2, B7, C1, C2 and C7 are drawn with the Generic Mapping Tool (Wessel et al. 2013).

Competing interests

The authors declare that they have no competing interests.

Received: 30 January 2016 Accepted: 7 June 2016

Published online: 28 June 2016

References

- Brandt S (1970) Statistical and computational methods in data analysis. North-Holland Publishing Company, Amsterdam
- Burton RK, McPherron RL, Russell CT (1975) An empirical relationship between interplanetary conditions and Dst. *J Geophys Res* 80:4204–4214. doi:10.1029/JA080i031p04204
- Chen CK, Wolf RA, Harel M, Karty JL (1982) Theoretical magnetograms based on quantitative simulation of a magnetospheric substorm. *J Geophys Res* 87:6137–6152. doi:10.1029/JA087iA08p06137
- Christensen EF, Lühr H, Hulot G (2006) Swarm: a constellation to study the Earth's magnetic field. *Earth Planets Space* 58:351–358. doi:10.1186/BF03351933
- Cowley SWH, Hughes WJ (1983) Observation of an IMF sector effect in the Y-magnetic field component at geostationary orbit. *Planet Space Sci* 31:73–90. doi:10.1016/0032-0633(83)90032-6
- Crooker NU, Siscoe GL (1981) Birkeland currents as the cause of the low-latitude asymmetric disturbance field. *J Geophys Res* 86:11201–11210. doi:10.1029/JA086iA13p1120
- De Michelis P, Daglis IA, Consolini G (1999) An average image of proton plasma pressure and of current systems in the equatorial plane derived from AMTE/CCE-CHEM measurements. *J Geophys Res* 104:28615–28624. doi:10.1029/1999JA900310
- Farthing WH, Sugiura M, Ledley BG, Cahill LJ Jr (1981) Magnetic field observations on DE-A and -B. *Space Sci Instrum* 5:551–560
- Finlay CC, Olsen N, Tøffner-Clausen LT (2015) DTU candidate field models for IGRF-12 and the CHAOS-5 geomagnetic field model. *Earth Planets Space* 67:114–131. doi:10.1186/s40623-015-0274-3
- Iyemori T (1990) Storm-time magnetospheric currents inferred from mid-latitude geomagnetic field variations. *J Geomag Geoelect* 42:1249–1265. doi:10.5636/jgg.42.1249
- Kamide Y, Baumjohann W, Daglis IA, Gonzalez WD, Grande M, Joselyn JA, McPherron RL, Phillips JL, Reeves EGD, Rostoker G, Sharma AS, Singer HJ, Tsurutani BT, Vasyliunas VM (1998) Current understanding of magnetic storms: storm-substorm relationships. *J Geophys Res* 103:17705–17728. doi:10.1029/98JA01426
- Kivelson MG, Russell C (1995) Introduction to space physics. Cambridge University Press, Cambridge
- Kunagu P, Balasis G, Lesur V, Chandrasekhar E, Papadimitriou C (2013) Wavelet characterization of external magnetic sources as observed by CHAMP satellite: evidence for unmodelled signals in geomagnetic field models. *Geophys J Int* 192:946–950. doi:10.1093/gji/ggs093
- Langel RA, Sweeney RE (1971) Asymmetric ring current at twilight local time. *J Geophys Res* 76:4420–4427. doi:10.1029/JA076i019p04420
- Lesur V, Macmillan S, Thomson A (2005) A magnetic field model with daily variations of the magnetospheric field and its induced counterpart in 2001. *Geophys J Int* 160:79–88. doi:10.1111/j.1365-246X.2004.02479.x
- Lesur V, Rother M, Wardinski I, Schachtschneider R, Hamoudi M, Chambodut A (2015) Parent magnetic field models for the IGRF-12GFZ-candidates. *Earth Planets Space* 67:87. doi:10.1186/s40623-015-0239-6
- Li H, Wang C, Kan JR (2011) Contribution of the partial ring current to the SYMH index during magnetic storms. *J Geophys Res* 116:A11222. doi:10.1029/2011JA016886
- Liemohn MW, Kozyra JU, Jordanova VK, Khazanov GV, Thomsen MF, Cayton TE (1999) Analysis of early phase ring current recovery mechanisms during geomagnetic storms. *Geophys Res Lett* 25:2845–2848. doi:10.1029/1999GL900611
- Liemohn MW, Kozyra JU, Thomsen MF, Roeder JL, Lu G, Borovsky JE, Cayton TE (2001) Dominant role of the asymmetric ring current in producing the stormtime Dst*. *J Geophys Res* 106:10883–10904. doi:10.1029/2000JA000326
- Lühr H, Maus S (2010) Solar cycle dependence of quiet-time magnetospheric currents and a model of their near-Earth magnetic fields. *Earth Planets Space* 62:843–848. doi:10.5047/eps.2010.07.012
- Lühr H, Kervalishvili G, Michaelis I, Rauberg J, Ritter P, Park J, Merayo JMG, Brauer P (2015) The interhemispheric and F region dynamo currents revisited with the Swarm constellation. *Geophys Res Lett* 42:3069–3075. doi:10.1002/2015GL063662
- Maus S, Lühr H (2005) Signature of the quiet-time magnetospheric magnetic field and its electromagnetic induction in the rotating Earth. *Geophys J Int* 162:755–763. doi:10.1111/j.1365-246X.2005.02691.x
- Nakano S, Iyemori T (2003) Local time distribution of net field-aligned currents derived from high-altitude satellite. *J Geophys Res* 108:1314. doi:10.1029/2002JA009519
- Newell PT, Sibeck DG, Meng C-I (1995) Penetration of the interplanetary magnetic field B_y and magnetosheath plasma into the magnetosphere: implications for the predominant magnetopause merging site. *J Geophys Res* 100:235–243. doi:10.1029/94JA02632
- Olsen N, Hulot G, Sabaka TJ (2007) The present field. In: Kono M (ed) Treatise on geophysics, vol 5. Elsevier, Amsterdam
- Olsen N, Lühr H, Finlay CC, Sabaka TJ, Michaelis I, Rauberg J, Tøffner-Clausen L (2014) The CHAOS-4 geomagnetic field model. *Geophys J Int* 197:815–827. doi:10.1093/gji/ggu033

- Papitashvili VO, Christiansen F, Neubert T (2002) A new model of field-aligned currents derived from high-precision satellite magnetic field data. *Geophys Res Lett* 29:1683. doi:[10.1029/2001GL014207](https://doi.org/10.1029/2001GL014207)
- Park J, Lühr H, Stolle C, Rother M, Min KW, Chung JK, Kim JH, Michaelis I, Noja M (2009) Magnetic signatures of medium-scale traveling ionospheric disturbances as observed by CHAMP. *J Geophys Res* 114:2156–2202. doi:[10.1029/2008JA013792](https://doi.org/10.1029/2008JA013792)
- Russell CT, McPherron RL (1973) Semiannual variation of geomagnetic activity. *J Geophys Res* 78:92–108. doi:[10.1029/JA078i001p00092](https://doi.org/10.1029/JA078i001p00092)
- Sabaka TJ, Olsen N, Purucker M (2004) Extending comprehensive models of the Earth's magnetic field with Oersted and CHAMP data. *Geophys J Int* 159:521–547. doi:[10.1111/j.1365-246X.2004.02421.x](https://doi.org/10.1111/j.1365-246X.2004.02421.x)
- Sabaka TJ, Olsen N, Tyler RH, Kuvshinov A (2015) CM5, a pre-Swarm comprehensive geomagnetic field model derived from over 12 yr of CHAMP, Ørsted, SAC-C and observatory data. *Geophys J Int* 200:1596–1626. doi:[10.1093/gji/ggu493](https://doi.org/10.1093/gji/ggu493)
- Sun W, Ahn BH, Akasofu SI, Kamide Y (1984) A comparison of the observed mid-latitude magnetic disturbance fields with those reproduced from the high-latitude modeling current system. *J Geophys Res* 89:10881–10889. doi:[10.1029/JA089iA12p10881](https://doi.org/10.1029/JA089iA12p10881)
- Thébault E, Hemant K, Hulot G, Olsen N (2009) On the geographical distribution of induced time-varying crustal magnetic fields. *Geophys Res Lett* 36:L01307. doi:[10.1029/2008GL036416](https://doi.org/10.1029/2008GL036416)
- Tsyganenko NA (2013) Data-based modelling of the Earth's dynamic magnetosphere: a review. *Ann Geophys* 31:1745–1772. doi:[10.5194/angeo-31-1745-2013](https://doi.org/10.5194/angeo-31-1745-2013)
- Turner NE, Baker DN, Pulkkinen TI, Roeder JL, Fennell JF, Jordanova VK (2001) Energy content in the storm time ring current. *J Geophys Res* 106:19149–19156. doi:[10.1029/2000JA003025](https://doi.org/10.1029/2000JA003025)
- Vennerstrom S, Christiansen F, Olsen N, Moretto T (2007) On the cause of IMF By related mid- and low latitude magnetic disturbances. *Geophys Res Lett* 34:L16101. doi:[10.1029/2007GL030175](https://doi.org/10.1029/2007GL030175)
- Wanliss JA, Showalter KM (2006) High-resolution global storm index: Dst versus SYM-H. *J Geophys Res* 111:A02202. doi:[10.1029/2005JA011034](https://doi.org/10.1029/2005JA011034)
- Wessel P, Smith WHF, Scharroo R, Luis JF, Wobbe F (2013) Generic Mapping Tools: improved version released. *EOS Trans AGU* 94:409–410. doi:[10.1002/2013EO450001](https://doi.org/10.1002/2013EO450001)
- Yamashita S, Iyemori T, Nakano S, Kamei T, Araki T (2002) Antisunward net Birkeland current system deduced from the Oersted satellite observation. *J Geophys Res* 107:1263. doi:[10.1029/2001JA900160](https://doi.org/10.1029/2001JA900160)

Submit your manuscript to a SpringerOpen® journal and benefit from:

- Convenient online submission
- Rigorous peer review
- Immediate publication on acceptance
- Open access: articles freely available online
- High visibility within the field
- Retaining the copyright to your article

Submit your next manuscript at ► [springeropen.com](https://www.springeropen.com)
